

Partially Diluted Zones in Dissimilar Cladding with AWS ER NiCrMo-3 Alloy Deposited by the MIG Process on ASTM A36 Steel: Analysis and Characterization by EBSD

W. C. Silva^{a*}, R. M. Nascimento^a, A. B. G. Nascimento^a, A. M. Mendes^a,

N. A. Castro^b, C. L. M. Silva^c

^aUniversidade Federal do Rio Grande do Norte, Programa de Pós-Graduação em Ciência e Engenharia de Materiais (PPGCEM), Natal, RN, Brasil.

^bUniversidade Federal do Rio Grande do Norte, Programa de Pós-Graduação em Engenharia Mecânica (PPGEM), Natal, RN, Brasil.

^cUniversidade da Amazônia, Departamento de Engenharia Mecânica, Belém, PA, Brasil.

Received: October 06, 2023; Revised: January 24, 2024; Accepted: March 16, 2024

The demand for oil and its derivatives has driven the oil and gas sector to explore deep waters. Nickel-based alloys, like Inconel, are used due to their corrosion resistance properties. Cladding structural steels with these alloys is a cost-effective solution. However, dissimilar metal welding poses challenges, including the formation of Partially Diluted Zones (PDZ). This work highlights the use of Electron Backscatter Diffraction (EBSD) as a very adequate technique for the microstructural characterization of dissimilar anticorrosive materials. The MIG process was utilized to perform cladding of Inconel 625 onto the A36 steel substrate. The samples were prepared for analysis using techniques such as EDS, FEG-SEM, EBSD, and Vickers microhardness testing. The results demonstrate the effectiveness of the EBSD technique in characterizing dissimilar metal cladding. The combination of EBSD with EDS analysis and microhardness testing provided comprehensive insights into the microstructure and mechanical properties of the material. EDS mapping analysis confirmed the formation of PDZ with a distinct beach-like morphology, indicating localized compositional variations. The uniform thickness of the PDZ, approximately 20 μm , highlights the convective motion and solidification behavior of the partially diluted zone. Phase map EBSD analysis revealed different crystal structures in the cladding zone, including a FCC structure for the nickel cladding layer and a BCC structure for the ferritic steel base metal. The PDZ exhibited the same crystal structure as the base metal, indicating chemical element diffusion without altering the ferritic steel structure. Contrast band EBSD analysis provided detailed microstructural information, revealing solidification structures and potential hardness variations. The observed martensite formation in the PDZ highlights its susceptibility to cracking and detachment of the coated layer. The hardness results support the microstructural findings, demonstrating significant variations in hardness across the cladding structure, particularly in the PDZ and at the interface between the Inconel alloy and the base metal. These findings contribute valuable insights into the microstructural and compositional gradients within the joint region, reinforcing their implications for material performance.

Keywords: Inconel 625, Dissimilar Welding, PDZ, EBSD.

1. Introduction

The search for greater production efficiency and meeting the growing demand for oil and its derivatives has led the oil and gas sector to explore deep and ultra-deep waters in the coastal zone of Brazil. With the discovery of oil reservoirs in the pre-salt layer and considering the geographic and geological characteristics of these fields, such as distance from the coastline, water depth, and well drilling, oil exploration has become one of the major engineering challenges due to the environment and conditions to which the equipment and components are subjected¹.

The corrosive aggressiveness of the environment in this type of activity requires the use of materials with excellent corrosion resistance properties such as nickel-based alloys. However, due to the high cost of these materials, the solution for employing this class of steels is the cladding of structural steels with nickel-based superalloys, such as Inconel 625 (NiCrMo-3)².

The use of the NiCrMo-3 superalloy deposited by welding aims to optimize the cost/benefit ratio in manufacturing components for special applications since the deposition is performed in specific areas. Thus, cladding for anticorrosion protection is mainly employed in pipelines and equipment,

*e-mail: williamcs09@gmail.com

and its main characteristic is the deposition of one or more layers of the corrosion-resistant alloy on the surface of the structural steel component/equipment³.

Nevertheless, dissimilar metal welding is a complex manufacturing process with significant challenges, such as controlling dilution and the formation of meta-stable microconstituents²⁻⁴. This procedure of cladding metals with distinct structural characteristics is characterized by forming a gradient in chemical composition and mechanical properties along the cross-section, which may render the interfacial region between the substrate and the cladding brittle and prone to fracture. This behavior has attracted great interest and scientific investigations⁵.

These microstructural changes are directly related to the heat input, compositional gradient, and the formation of critical regions with high hardness, sometimes associated with issues such as delamination of the cladding layer, loss of toughness, and corrosion phenomena^{6,7}. Thus, after solidification of the liquid mass, Type II boundaries (longitudinal to the fusion line) and PDZ are frequently observed, with the latter resulting from the partial diluting between the filler metal and the base metal with differences in their chemical compositions^{8,9}.

The attenuation of this metallurgical phenomenon is of great interest to industry and literature. Despite providing numerous information on dissimilar metal cladding and even with great contributions from previous research, investigations in the same line of deepening on the influence and mechanisms of formation of Partially Diluted Zones are necessary^{10,11}.

More precise characterization techniques, such as EBSD, have been employed in the study and characterization of dissimilar cladding, considering their potential to reveal the microstructure without the use of metallographic reagents. Thus, the EBSD technique involves obtaining phase orientation maps, enabling to identify grain orientations and geometry. These maps provide the reference stereographic triangle used in identifying crystallographic planes, with each color corresponding to a plane parallel to the scanning surface^{12,13}.

Therefore, the present study aims to employ the EBSD technique and microhardness analysis to analyze and identify phases, as well as the microstructural characterization of the joint region between an ASTM A36 base metal and an Inconel 625 deposited by MIG cladding. The goal is to obtain more precise and reliable results to better understand the formation mechanisms of PDZs.

2. Experimental Characterization

The base metal (BM) used as a substrate was ASTM A36 steel with a thickness of 3/8 in, width of 5 in, and length of 8 in. The filler metal (FM) used was the AWS ER-NiCrMo-3 alloy wire electrode (Inconel 625) with a diameter of 1.2 mm. The chemical compositions of the BM and FM are presented in Table 1.

The cladding parameters for the deposition of a single layer are indicated in Table 2.

The samples were collected by cold cutting using a band saw from the cladded plate, followed by grinding (180 to 1200 mesh), diamond suspension polishing (6, 3, and 1 μm), and finally precision polishing using a colloidal silica suspension of 0.04 μm .

The macrograph was obtained using a camera, and the area measurements were conducted using the ImageJ application. Subsequently, the global dilution was calculated following Equation 1¹⁴.

$$D = \frac{A_{bm}}{A_{bm} + A_{fm}} \quad (1)$$

The microstructure of the cladding zone was analyzed using Field Emission - Scanning Electron Microscopy (FE-SEM) on an Auriga 40 from ZEISS. EBSD was performed with a Bruker E-Flash device attached to the same FE-SEM equipment. The sample surface was tilted at an angle of 70° relative to the horizontal, and the scanning step size in the image was approximately 0.45 μm . The acceleration voltage was set at 25 kV, probe current at 20 μA , and working distance at 15 mm. Chemical composition was evaluated by Energy Dispersive X-ray Spectroscopy (EDS) and the

Table 1. Chemical composition (by weight percent) of ASTM A36 steel and AWS ER NiCrMo-3 (Inconel 625) welding wire.

Material	wt. %	C	Co	Fe	Mn	Al	Ni	Cr	Cu	S	Si	P
A36	Min.	0a25		98	0.6				0.2	0	0	0.2
	Max.	0.28			0.9					0.05	0.04	
Inconel 625	Min.	0	0.84	0	0	0	58	20		0	0	
	Max.	0.1	1	5	0.50	0.4	64.9	23		0.015	0.50	0.015

Table 2. MIG cladding parameters.

Cladding Parameters		
Voltage [V]	27	
Stickout [mm]	17	
Welding Speed [mm/min]	300	
Wire Feed Speed [m/min]	6	
Heat Input [J/mm]	31.0	
Interpass Temperature [°C]	<100	
Shielding gas	Type	Argon
	Purity [%]	99.998
	Flow Rate [L/min]	15

mechanical behavior of the samples was tested using Vickers microhardness by a FM-810 from Future Tech according to the ASTM E 384 standard¹⁵.

3. Results and Discussion

With the macro image obtained, as shown in Figure 1, global dilution was calculated from the macrographs using the relationship between areas (Equation 1). This calculation involved the ratio of the amount of fusion base metal, as observed in Figure 2a (region Abm), contained in the filler metal shown in Figure 2b (region Afm). The resulting global dilution was determined to be 12.09%, in accordance with studies published by Kejelin et al.¹⁶, Jorge et al.¹⁷, and Alvarães et al.¹⁸. These studies reported, in the GMAW process, a percentage greater than 10.0%.

Compositional mappings by EDS are illustrated in Figure 3.

As shown in Figure 3a, the low-alloy steel underwent dilution by the Inconel cladding layer, exhibiting PDZ forming a beach-like morphology because of the different melting temperatures of the nickel alloy (~1350 °C), which is lower than that of steel (~1500 °C). Additionally, no metallurgical discontinuities such as porosity or lack of fusion were observed in the Bonding Zone (BZ). These characteristics indicate that there is good adhesion between the cladding layer and the base metal.

The chemical composition of PDZ primarily consists of Fe, Cr, and Ni, as determined through semi-quantitative EDS analysis, as illustrated in Figure 4. No other elements were detected through chemical analysis, and there were no

precipitated phases observed in the micrographs. The result was derived from the average of compositional values obtained at eight different points in the PDZ, as presented in Table 3.

In the study conducted by Silva¹⁹, it was observed that the application of higher heat inputs during the welding process resulted in a reduction in the quantity of PDZs, as per his measurements. However, the reliability of this parameter was questioned based on research presented by Kejelin¹⁰. This latter author demonstrated that, even when subjected to the same heat input, the weld beads can exhibit completely distinct geometric characteristics. This suggests that the amount of heat is not a reliable indicator for this purpose, as variations in geometry are also associated with fluctuations in convective movements within the melt pool, identified as the predominant mechanism for the occurrence of the PDZs. Furthermore, Kejelin¹⁰ cautioned that the use of high welding energies can lead to a significant increase in dilution levels, depending on other welding parameters, necessitating the deposition of additional layers and consequently raising manufacturing costs.

The morphologies of PDZs are determined by the convective movement promoted by the weld pool in contact with the partially melted substrate, due to the thermal input and subsequent solidification of the partially mixed substrate^{20,21}. However, the present work observed that the formation of PDZs does not occur in a continuous and linear way along the fusion line. There are preferential regions that can contribute to the formation of macrosegregations with thicknesses of the order of 20 µm.

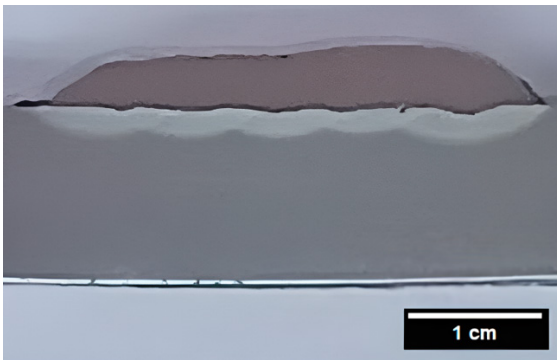


Figure 1. Macrograph of the cross section of the coated component.

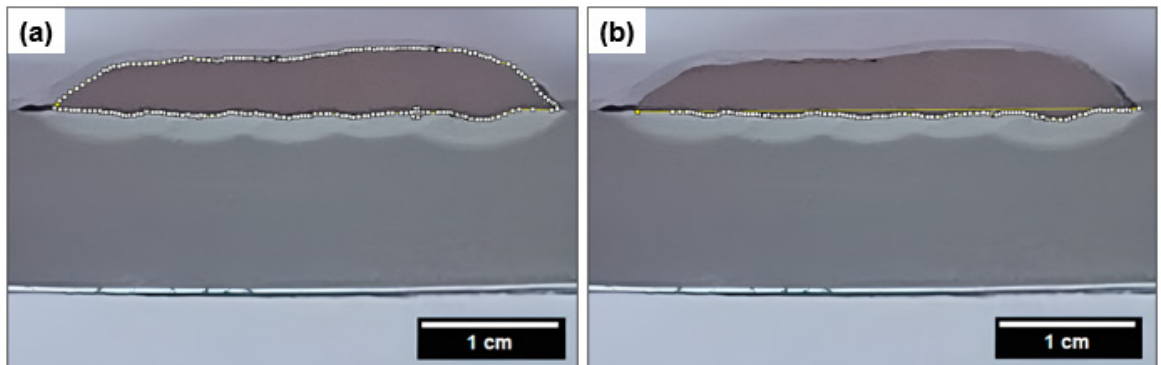


Figure 2. Macrograph with area delimitation markings for calculating global dilution using ImageJ.

Table 3. EDS point analysis of a cladding-welded sample.

Element	Wt. 1 (%)	Wt. 2 (%)	Wt. 3 (%)	Wt. 4 (%)	Wt. 5 (%)	Wt. 6 (%)
Fe	84.78	86.1	82.9	86.04	87.06	86.04
Cr	1.13	1.04	1.04	1.01	1.03	1.00
Ni	2.48	2.45	2.86	2.61	2.62	3.40
Element	Wt. 7 (%)	Wt. 8 (%)	Wt. 9 (%)	Wt. 10 (%)	Wt. 11 (%)	Wt. 12 (%)
Fe	82.09	77.92	76.72	66.79	57.05	71.28
Cr	1.77	2.19	3.26	4.4	6.23	4.17
Ni	5.42	7.04	10.56	14.5	21.16	11.85
Average	67.96		4.52		14.52	
Standard error	Fe	6.04	Cr	0.86	Ni	3.32

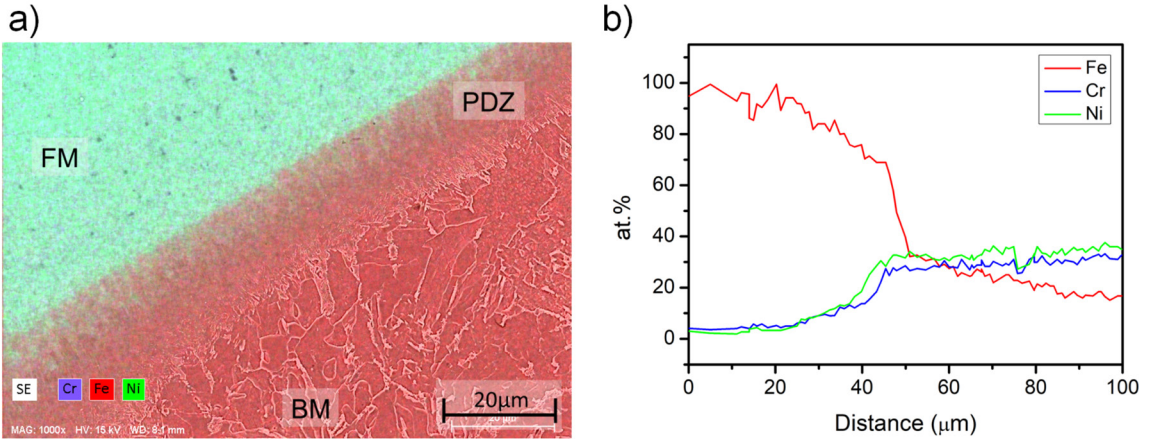


Figure 3. EDS analysis of the cross-section of the cladding region, (a) by mapping and (b) by line scan across the PDZ.

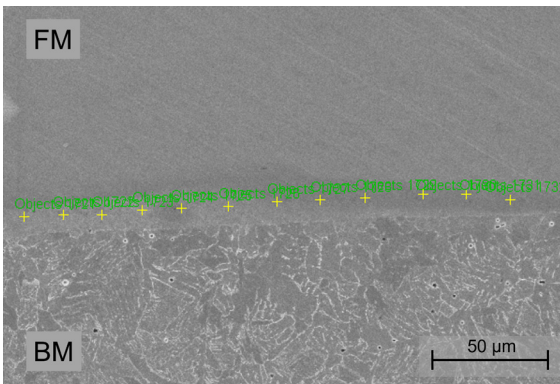


Figure 4. Semi-quantitative EDS analysis.

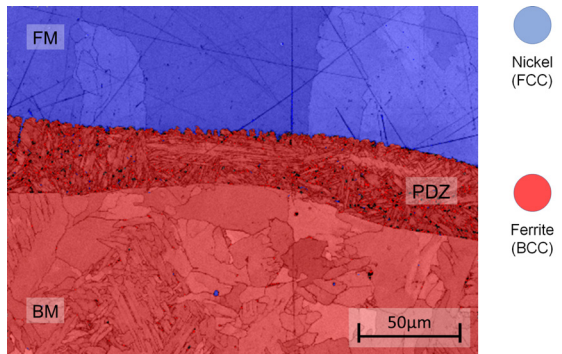


Figure 5. EBSD phase map of the cladding zone.

The micrograph illustrated in Figure 5 was generated by EBSD and shows the compositional mapping in terms of the sample phase in the welding region.

Different from the traditional SEM analysis, Figure 5 was obtained from measuring the diffraction patterns of electrons that are backscattered from a sample surface and consequent determination of the crystalline structures of individual grains. The blue region corresponds to the FCC structure of the nickel cladding layer, with 36.5%, while the red region refers to the ferritic BCC structure of the steel, with 62.9%, and the martensite formed at the interface of the coated component. Therefore, two regions with different microstructures can be seen in the red area. The first is a thin layer adjacent to the blue region with acicular microstructure consisting of the PDZ and the second region refers to the base metal (A36 steel) in the part below the micrograph. As the PDZ has the same crystalline structure as the base metal and considering the results of EDS in the formation of dissolution gradients in this zone, it is assumed that the diffusion of chemical elements only modifies the chemical composition, and does not affect the structure of the ferritic base structure of the steel.

Figure 6a shows the image of the contrast band (CB) map generated by EBSD in the bonding region between the coating and the base metal.

When compared to the image generated by scanning electron microscopy in the same region (Figure 6b), the

level of detail in the microstructure is notable, with good definition of the beach morphology, even more evident than that observed in the EDS image (Figure 3a).

The CB maps enhance grain boundaries by relating the average intensity of Kikuchi bands to the total intensity within the region of interest, thus providing a qualitative analysis of the microstructure. Due to the heat input associated with the welding process, equiaxed grains, acicular ferrite and bainite are observed in the HAZ. Indicating a heat treatment in this region, with a cooling rate sufficient to favor the formation of metastable microconstituents resulting from diffusion and shear processes (bainite), nucleated at the boundaries and propagate towards the center of the grain. Furthermore, it is possible to identify the presence of martensite in the PDZ. The formation of this martensite in this composition range occurs mainly due to increased hardenability, resulting from the enrichment of chemical elements that stabilize austenite, such as nickel (Ni), manganese (Mn) and cobalt (Co), present in the Inconel alloy 625. The high level of microstructural detail provided by EBSD-BC can aid in predicting the material's behavior under service conditions because, considering the presence of martensite in the PDZ and the consequent possible high hardness in this region, it is possible to predict the susceptibility to cracking phenomena, and consequently detachment of the coated layer.

The microhardness distribution from the A36 base metal to the Inconel cladding layer is shown in Figure 7.

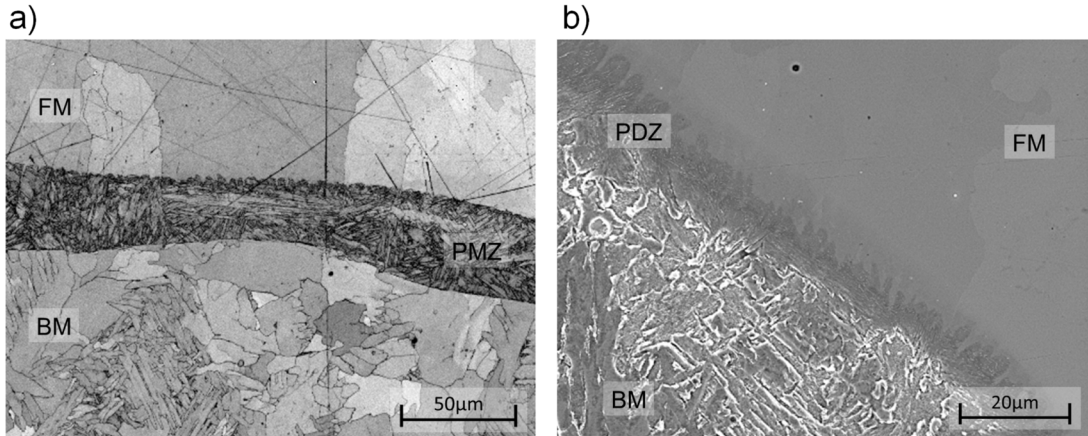


Figure 6. Cross-section of the cladding zone imaging by (a) EBSD band contrast map and (b) scanning electron microscopy (SEM).

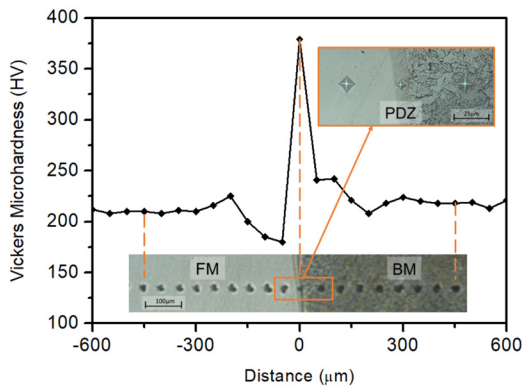


Figure 7. Microhardness distribution from the A36 base metal to the Inconel 625 cladding layer.

Figure 7 illustrates the micro-hardness measurements along the cross-section. The base metal showed a hardness of approximately 211 HV, which gradually increased towards the interface. The hardness reached 225 HV at a distance of 200 µm from the interface. There was a subsequent gradual decline, reaching a minimum value of 180 HV at 50 µm from the interface. These variations can be attributed to microstructural and compositional changes in the base metal's HAZ.

A significant hardness transition was observed in the PDZ, where the hardness significantly increased to 379 HV. This increase can be attributed to the formation of martensite and the presence of a finer grain structure compared to the base metal, as confirmed by EBSD analysis. Additionally, the Inconel alloy adjacent to the interface exhibited a hardness of 241 HV, likely influenced by carbon migration. The hardness gradually decreases as you move away from the interface, and stabilizes at approximately 220 HV, which is characteristic of Inconel alloys.

Similar findings were reported by Cavalcante et al.²² in their study on Inconel 625 coatings deposited on ASTM A387 structural steel using MAG welding. They observed a sharp increase in hardness immediately after the zero line, with values around 220 HV in the coating region (Inconel 625) and approximately 330 HV in regions close to the substrate-coating interface.

4. Conclusion

The use of EBSD technique in characterizing dissimilar metals after cladding was demonstrated. The combination of EBSD with EDS analysis and microhardness testing provided detailed information about the microstructure of the material, enabling to better understand the formation mechanisms of the PDZs.

EDS mapping analysis confirmed the formation of PDZ with a beach-like morphology in the cladding zone. Good adhesion between the Inconel cladding layer and the low-alloy steel base metal was observed without any metallurgical discontinuities. The PDZ thickness was uniform at approximately 20 µm, highlighting the convective motion and solidification behavior of the partially diluted substrate.

Phase map EBSD analysis identified different crystal structures in the cladding zone: a FCC structure corresponding to the nickel cladding layer and a BCC structure representing the ferritic steel base metal. The PDZ, located between the cladding layer and the base metal, exhibited the same crystal structure as the base metal. Chemical element diffusion within the PDZ affected the composition without altering the ferritic steel structure.

Contrast band EBSD analysis provided more detailed microstructural information, surpassing SEM and EDS imaging. It revealed the morphology of the transition zone known as “beach”, and improved the visibility of grain boundaries. Using CB, it was possible to clearly visualize the microstructure in the solidification region (cladding). In the PDZ, where the formation of martensite was evidenced. As well as in the BM, where equiaxed grains, acicular ferrite and bainite were identified.

The presence of martensite in the PDZ signals a potential for increased hardness, as well as making the coated layer more susceptible to cracking and detachment. Therefore, EBSD-BC analysis proves to be a valuable tool for predicting material behavior in service conditions.

The hardness results confirmed the predictions based on the microstructural analysis conducted via EBSD. The significant variations in hardness observed in the cladding structure, particularly in the PDZ with martensite formation and finer grain structure, along with the elevated hardness at the interface between the Inconel alloy and the base metal,

validate the findings and provide valuable insights into the microstructural and compositional gradients within the joint region, reinforcing their implications for material performance.

5. Acknowledgments

The authors would like to thank the *Coordenação de Aperfeiçoamento de Pessoal de Nível Superior (CAPES)* for the financial support provided for developing this research work.

6. References

- Petrobras [homepage on the Internet]. Rio de Janeiro; 2023 [cited 2023 Oct 6]. Available from: <https://petrobras.com.br/>
- Zhang Q, Tang R, Yin K, Luo X, Zhang L. Corrosion behavior of Hastelloy C-276 in supercritical water. *Corros Sci.* 2009;51(9):2092-7. <http://dx.doi.org/10.1016/j.corsci.2009.05.041>.
- Wang JF, Sun QJ, Wang H, Liu JP, Feng JC. Effect of location on microstructure and mechanical properties of additive layer manufactured Inconel 625 using gas tungsten arc welding. *Mater Sci Eng A.* 2016;676:395-405. <http://dx.doi.org/10.1016/j.msea.2016.09.015>.
- Deacon RM, DuPont JN, Marder AR. High temperature corrosion resistance of candidate nickel-based weld overlay alloys in a low NOx environment. *Mater Sci Eng A.* 2007;460-461:392-402. <http://dx.doi.org/10.1016/j.msea.2007.01.150>.
- Constantino WS. Avaliação microestrutural de Zonas Parcialmente Diluídas obtidas por soldagem dissimilar empregando os metais de adição Inox 309L e Inconel 625 [dissertation]. Natal: Programa de Pós-graduação em Ciência e Engenharia de Materiais, Universidade Federal do Rio Grande do Norte; 2018.
- Rowe MD, Nelson TW, Lippold JC. Hydrogen induced cracking along the fusion boundary of dissimilar metal welds. *Weld J.* 1999;78(10):31-7.
- Wang Z, Xu B, Ye C. Study of martensite structures at the weld interface and fracture toughness of dissimilar metal joints. *Weld J.* 1993;72(8):397-402.
- Kou S. *Welding metallurgy*. Hoboken: John Wiley & Sons; 2003.
- Dupont JN, Lippold JC, Kiser SD. *Welding metallurgy of nickel-base alloys*. Hoboken: John Wiley & Sons; 2009.
- Kejelin NZ. Soldagem de revestimento de aços comuns C-Mn com superliga a base de níquel Inconel 625 [thesis]. Florianópolis: Programa de Pós-graduação em Engenharia Mecânica, Universidade Federal de Santa Catarina; 2012.
- Kou S, Yang YK. Fusion-boundary macrosegregation in dissimilar-filler welds. *Weld J.* 2007;86:303s-12s.
- Beaugrand VCM, Smith LS, Gittos MF. Subsea dissimilar joints: failure mechanisms and opportunities for mitigation. In: *Corrosion 2009*; 2009; Atlanta, GA. Proceedings. Houston: Nace International; 2009. 12 p.
- Fischer RR. Preparação e caracterização por EBSD e indentação instrumentada de superfícies após tratamentos de nitretação por plasma do aço inoxidável AISI 304 [dissertation]. Joinville: Universidade do Estado de Santa Catarina; 2017.
- Lippold JC, Kiser SD, DuPont JN. *Welding metallurgy and weldability of nickel-base alloys*. Hoboken: John Wiley & Sons; 2011.
- ASTM: American Society for Testing and Materials. ASTM E384-22: standard test method for microindentation hardness of materials. West Conshohocken: ASTM; 2022.
- Kejelin NZ, Almeida Buschinelli AJ, Bohórquez CEN. Soldagem dissimilar do aço X-60 com Inconel 625. Florianópolis: UFSC; 2006.
- Jorge JC, Meira OG, Madalena FCA, Souza LFG, Araujo LS, Mendes MC. Evaluation of the AISI 904L alloy weld overlays obtained by GMAW and electro-slag welding processes. *J Mater Eng Perform.* 2017;26(5):2204-12. <http://dx.doi.org/10.1007/s11665-017-2631-9>.
- Alvarães CP, Madalena FCA, Souza LFGD, Jorge JCF, Araújo LS, Mendes MC. Performance of the INCONEL 625 alloy weld overlay obtained by FCAW process. *Materia.* 2019;24(1):e12290. <http://dx.doi.org/10.1590/s1517-707620190001.0627>.
- Silva CC. Revestimentos de ligas de níquel depositadas pelo processo GTAW com alimentação de arame frio: aspectos operacionais e metalúrgicos [tese]. Fortaleza: Programa de Pós-graduação em Engenharia de Materiais e Metalúrgica, Universidade Federal do Ceará; 2011.
- Soysal T, Kou S, Tat D, Pasang T. Macrosegregation in dissimilar-metal fusion welding. *Acta Mater.* 2016;110:149-60. <http://dx.doi.org/10.1016/j.actamat.2016.03.004>.
- Yang YK, Kou S. Macrosegregation in Cu-30Ni welds made with dissimilar filler metals. *Sci Technol Weld Join.* 2008;13(4):318-26. <http://dx.doi.org/10.1179/174329307X213738>.
- Cavalcante NE, Andrade TC, Pinheiro PHM, Miranda HC, Motta MF, Aguiar WM. Estudo de procedimentos de soldagem MIG/MAG para aplicação de revestimentos de liga de níquel Inconel 625 em aço estrutural ASTM A387 Gr.11. *Soldag Insp.* 2016;21(1):70-82. <http://dx.doi.org/10.1590/0104-9224/S12101.07>.